J Mater Sci **(2023) 58:7583–7593**

Chemical routes to materials

A study of size-controlled Au@Cu_2O nanocomposite for highly improved methyl orange catalytic performances

Yun-Qi Dou[1], Tian-Song Deng[1,*], Qi Zhang[1], Xiaoyu Zhao[2], Jia Liu[2], and Zhiqun Cheng[1]

[1] *School of Electronics and Information Engineering, Hangzhou Dianzi University, Hangzhou 310018, People's Republic of China*
[2] *College of Materials and Environmental Engineering, Hangzhou Dianzi University, Hangzhou 310018, People's Republic of China*

Received: 30 December 2022
Accepted: 21 April 2023

ABSTRACT

In this study, we synthesized Au-Cu_2O core–shell nanoparticles (Au@Cu_2O NPs) with epitaxial Cu_2O shell, which have highly improved catalytic performances in methyl orange reduction reaction. We have obtained Au@Cu_2O NPs with different sizes at low temperatures by changing the amount of Cu^{2+} precursor. Both Au and Cu_2O are catalytic materials, especially Cu_2O, as a *p*-type semiconductor, whose catalytic ability depends on the crystalline facets. Catalytic reduction of methyl orange (MO) was used as a model system to explore the catalytic properties of Au@Cu_2O nanocomposite. In comparison to pure Au and Cu_2O NPs, the catalytic performance of Au@Cu_2O has a noticeable improvement. The best catalytic rate was ~ 22 times faster than that of AuNRs and ~ 4 times than that of Cu_2O NPs. By studying the catalytic mechanism, it is supposed that the Schottky barrier at the Au-Cu_2O interfaces leads to the charge separation, which is beneficial to catalysis. Therefore, the Au@Cu_2O NPs we designed with controllable shell thickness is an ideal composite material in the catalyst domain.

Introduction

At present, the property of single material has been incapable to meet the demand of actual applications, therefore hybrid nanostructures have obtained more attention from all kinds of fields. Usually, the composite materials not only keep their original functions of individual component but also have other synergistic effects, producing novel properties in the aspect of physics, chemistry, and bio-medicine [1–5]. What's more, compared to nanostructures with a single material, multi-component nanostructures are easier to improve their properties by changing the size, proportion, morphology, and geometry of

---

Handling Editor: Yaroslava Yingling.

Address correspondence to E-mail: dengts@pku.edu.cn

https://doi.org/10.1007/s10853-023-08524-1

different components [6–8]. Metal–semiconductor nanostructures have generated considerable research interests among the multi-component nanostructures, because the combination of metal and metal oxides induces electron enrichment phenomenon, which benefits charge separation [9, 10]. In addition, semiconductor materials have very low cost. Metal–semiconductor nanostructures can reduce production costs while they achieve the improved performances, in comparison to other hybrid nanostructures.

Decorating metal nanoparticles or supported by a novel metal core onto semiconductor materials, metal–semiconductor materials can be used in biological detection, catalysis, and other applications [11–14]. Au nanostructures have been widely used in catalysis, especially Au nanorods (AuNRs), having an excellent localized surface plasmon resonances (LSPRs) property, and their LSPRs can be precisely controlled by the aspect ratio (AR) [15–18]. In addition, Cu_2O, a p-type semiconductor, having distinguished optical, electronic, and catalytic properties [19–21], is similarly attracting more focus. Hence, numerous current experiments that study the morphology and properties of Au–Cu_2O hybrid nanostructures have been carried out [22–29].

In terms of property, the synergistic effect of Au–Cu_2O nanoparticles is influenced by the structure, morphology, size or growth mode of Au and Cu_2O. Lu's group [30] have designed gold nanospheres with hollow Cu_2O shell to control their optical properties, but the thin Cu_2O shell is irregular and incomplete. In addition, Au nanospheres as a core, which have the isotropic shape, cannot offer rich plasmonic modes. AuNRs covered by Cu_2O octahedra shell consisting of {111} facets with accurate size control have been synthesized by Kong et al. [31] to enhance the catalytic ability, but with the combination of the spectra and catalytic experiments, the physical properties of AuNRs cannot be fully utilized owing to the thick Cu_2O shell. Therefore, there is still plenty of scope for optimization of the morphology of Cu_2O shell. Xu's group [32] grew a series of Au-Cu_2O hybrid structures to study the internal energy transfer of the hybrids by generating the photocurrent, and found that the core–shell structures had better Schottky effect, which is benefit for electron transfer and can be used in the catalysis field.

In this paper, we obtained an Au–Cu_2O core–shell nanocomposite using large AuNRs to overgrow the thickness-suitable and even Cu_2O shell, which can supply a bigger contact area and more catalytic active sites. To improve the Cu_2O coverage rate, SDS and CTAB were used as binary surfactants. We also slowed down the reaction rate by changing the temperature of the growth solution from room temperature to 5 °C. And we controlled the Cu_2O shell thickness by changing the volume of Cu^{2+} precursor. Finally, by reducing methyl orange (MO) with the assistance of $NaBH_4$, we explored the catalytic performance of Au@Cu_2O nanostructure related to the thickness of Cu_2O and studied the corresponding catalytic mechanism.

Experimental

Chemicals

Hexadecyltrimethylammonium bromide (CTAB, > 99%) was purchased from TCI America. L-ascorbic acid (AA, > 99.99%), chloroauric acid ($HAuCl_4$), hydrochloric acid (HCl, 37 wt. % in water), copper (II) chloride dihydrate ($CuCl_2{\cdot}2H_2O$, 99.99%), sodium dodecyl sulfate (SDS, > 92.5%), hydroxylamine hydrochloride ($NH_2OH{\cdot}HCl$, 99.99%) and methyl orange (MO, 96%) were purchased from Shanghai Macklin Biochemical Technology Co., Ltd. Sodium borohydride ($NaBH_4$, 98%), sodium oleate (NaOL, > 99.8%), silver nitrate ($AgNO_3$, > 99.8%) were purchased from Shanghai Aladdin Biochemical Technology Co., Ltd. Sodium hydroxide (NaOH, > 96.0%), Ethanol (EtOH, > 99.7%) were purchased from Hangzhou Gaojing Fine Chemical Industry Co., Ltd. Ultrapure water (Millipore Milli-Q grade) with a resistivity of 18.2 MΩ was used in all of the experiments. All chemicals were used as received without further purification.

Synthesis of AuNRs

The AuNRs were synthesized using a previously reported "seed-mediated method" [33] with slightly modification. For the seed solution, 0.25 mL of 10.0 mM $HAuCl_4$ and 10 mL of 0.1 M CTAB were mixed in a 20 mL bottle. The freshly prepared ice-cold $NaBH_4$ (0.6 mL, 10.0 mM) was quickly added to the mixed solution under the vigorous agitation. After the solution became brownish yellow, the stirring was stopped and let the solution stand for about 30 min before use.

For the growth solution, 7.0 g of CTAB and 1.24 g of NaOL were added in a 500 mL flask, followed by the addition of 250 mL water, magnetically stirred and heated in 50 °C water bath until it's completely dissolved. The solution was cooled down to 30 °C, after which 24 mL of 4.0 mM $AgNO_3$ was added and kept it for 15 min. 25 mL of 10.0 mM $HAuCl_4$ and 225 mL of water were added and the solution was magnetically stirred at 700 rpm for 1 h until the color of solution faded. 1.5 mL of HCl (37 wt.% in water) was added under the stirring at 700 rpm for 15 min. After that, 1.25 mL of 64.0 mM AA was added and the mixture was vigorously stirred for 30 s. Finally, 0.4 mL of seed was injected into the mixture with stirring for 30 s. The subsequent rod growth was performed under static conditions overnight to obtain AuNRs. The resulting AuNRs have a LSPR wavelength of 752 nm. The final AuNRs was centrifuged at 8000 rpm for 15 min, washed once with water, and redispersed in 50 mL of 1.5 mM CTAB.

Synthesis of Au@Cu_2O NPs

The prepared AuNRs, dispersed in 1.5 mM CTAB, have a maximum of absorption peak about 1.35 when it is diluted 16.7 times in a 1 cm cuvette. Y μL of 0.05 M $CuCl_2 \cdot 2H_2O$ aqueous solution were added in X mL of 1.5 mM CTAB and followed by adding 0.5 mL of 0.3 M SDS. 0.3 mL of AuNRs solution was added and then the mixed solution was magnetically stirred (300 rpm, 10 min). The solution was kept static at 5 °C for 5 min. 65 μL of 0.1 M NaOH were added, followed by adding 175 μL of 0.1 M $NH_2OH \cdot HCl$. The solutions were mixed and stirred for 10 s. The mixture left undisturbed at 5 °C for 2 h. Then, the resulting solution was centrifuged at 4000 rpm for 5 min to remove the surfactant. The product was washed with deionized water once and ethanol twice, and stored in 1.5 mL ethanol. The thickness of the Cu_2O shell was controlled by changing the volume of the $CuCl_2$ solution. The value of y we chosen was 35 μL, 65 μL, and 100 μL, and the Au@Cu_2O NPs synthesized with three sizes was termed as AC-35, AC-65, and AC-100, respectively. X was adjusted to ensure 5 mL of the total volume.

Synthesis of Cu_2O NPs

The Cu_2O NPs were obtained by a method similar to getting Au@Cu_2O NPs. 65 μL of 0.05 M $CuCl_2 \cdot 2H_2O$ aqueous solution was added in 3.9 mL of water, followed by adding 0.5 mL of 0.3 M SDS. 0.3 mL of AuNRs solution was added with magnetically stirring at 300 rpm for 10 min. Let it undisturbed at 5 °C for 5 min. Afterward, 65 μL of 0.1 M NaOH was added, followed by adding 175 μL of 0.1 M $NH_2OH \cdot HCl$. The solutions were mixed and stirred for 10 s. The mixture was aged at 5 °C for 2 h. Then, the product was obtained by centrifugation and washed with deionized water once and absolute ethanol twice, and finally stored in 1.5 mL ethanol.

Catalytic reduction of MO

The prepared catalytic nanoparticles (AC-35/65/100, AuNRs, Cu_2O NPs) were centrifuged and uniformly dispersed in Milli-Q water by ultrasonication. In a cuvette, 1 mL of MO (0.1 mM) and 16 μL of catalyst were added, followed by the addition of a freshly prepared $NaBH_4$ (50 μL, 0.05 M) solution. After adding the catalyst, the solution gradually changed from orange to colorless, which was monitored by measuring the change in absorbance of MO at 464 nm by UV–vis spectra. The spectra were recorded for a regular interval time of 1 min. And each reaction has been repeated three times to minimize the test error.

FDTD calculations

The extinction spectra simulations of the Au@Cu_2O nanostructures were calculated using the finite-difference-time-domain (FDTD) method with a software package from FDTD Solutions (Lumerical Solutions, Inc.). The refractive index of the surrounding medium was taken to be the refractive index of water (1.33). The boundary conditions of the simulation are perfectly matched layer (PML). The boundary with NPs inside was divided into mesh size of 2 nm. A plane wave from 300 to 1200 nm wavelength was illuminated. The Au core in the Au@ Cu_2O NPs was modeled as a cylinder capped with two half spheres at both ends. And the Cu_2O shell was modeled as a cuboid with rounded corners and edges. For the longitudinal excitation, the incident light was perpendicular to the vertical axis and polarized along the long axis of gold nanorods. For the transverse excitation, both the incident light and polarization direction were perpendicular to the long axis. Dielectric functions for Au and Cu_2O were provided by Palik [34]. To investigate the influence of anisotropy on the extinction spectra, we also simulated the Au@Cu_2O with AR of 1, 2, 3, and 4, respectively.

Characterizations

Optical extinction spectra were recorded with a UV-1900i spectrophotometer (SHIMADZU, Japan) with a 1.0 cm optical path. The transmission electron microscope (TEM) images were obtained with a HT-7700 microscope (HITACHI, Japan) operated at 100 kV. High resolution TEM (HRTEM) images and energy disperse spectroscopy (EDS) mapping were performed by a Fei-Talos-F200S operated at 200 kV. The particle sizes of the nanoparticles were measured from TEM images, whereby > 50 nanoparticles were measured for each sample.

Results and discussion

The AuNRs used for further synthesis of Au@Cu_2O NPs were obtained by seed-mediated method with binary surfactant mixtures [33]. Their extinction spectra and morphology characterization are given in Figure S1 in the Supporting Information. The AuNRs sample with good monodispersity have an average length of 112 ± 9 nm and the AR of ~ 3, which have a narrow longitudinal peak at 752 nm. The synthetic process of Au@Cu_2O NPs was shown in Scheme 1. In the CTAB solution with $CuCl_2 \cdot 2H_2O$ as the source of copper, SDS surfactant, concentrated AuNRs solution, NaOH and $NH_2OH \cdot HCl$ were orderly added. $NH_2OH \cdot HCl$ was used as the reducing agent. When $NH_2OH \cdot HCl$ was added, small Cu_2O seed particles were formed. These seed particles quickly aggregated into larger particles and attached to the AuNRs [35]. After aging for 2 h, larger Cu_2O particles grow into the dense shell and the final product was obtained.

To cover a uniform Cu_2O shell, CTAB and SDS were used as binary surfactant mixtures, and the mixture solution needed to age in a refrigerator at 5 °C before adding $NH_2OH \cdot HCl$. The reason for choosing binary surfactant is that AuNRs are easy to aggregate during the process of magnetically stirring using SDS only, or at a low concentration of CTAB. Figure S2 show the results of using CTAB < 1 mM, indicating that the aggregated AuNRs cannot coat with intact Cu_2O shells on their surface. Lower temperature is designed to slow down the growth speed of Cu_2O shell, because Cu^{2+} was rapidly reduced to Cu_2O at room temperature, which is unfavorable for uniform coverage. At the lower temperature condition (5 °C), the change rate of solution color is apparently slow, and the final product has good monodispersity and uniform coverage.

The high-resolution transmission electron microscopy (HRTEM) image of a single Au@Cu_2O particle is shown in Fig. 1a. Obvious bright/dark contrast indicates that the Au nanorod locates in the center of the cubic particle. Figure 1b shows the enlarged picture of the red square region of Fig. 1a, which is the interface between Au core and Cu_2O shell on the body part of Au@Cu_2O, revealing oriented epitaxial growth and the single-crystal nature of Cu_2O shell. Cu_2O (200) is parallel to Au (200). The same TEM analysis was performed in Figure S3b, which chose the tips of the Au@Cu_2O nanoparticle in red square region of Figure S3a. Similarly, the {200} facets of Cu_2O grown along the {200} facets of Au. The FFT of Cu_2O shell in Fig. 1c reveals the Cu_2O shells are mainly constructed by {200} facets and {110} facets, which is owing to a larger concentration of $NH_2OH \cdot HCl$ added. The amount of $NH_2OH \cdot HCl$ may influence the growth rate of different facets [35], which have a crucial effect on the catalytic property. High-angle annular dark-field scanning transmission electron microscopy (HAADF-STEM) images of Au@Cu_2O nanoparticles are shown in Figure S3c. A core–shell structure that a light Cu_2O shell around a bright Au core was obviously exhibited. The elemental distribution of Au, Cu, and O from the

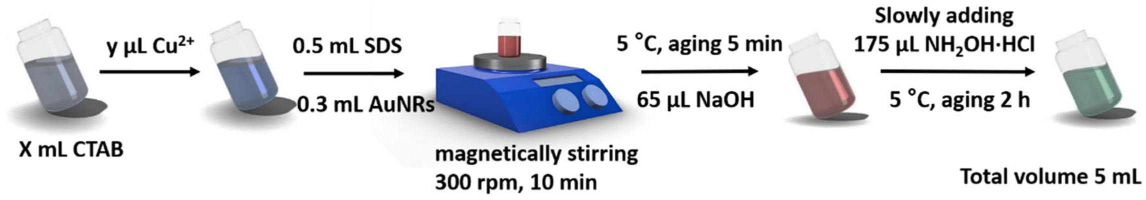

Scheme 1 Schematic illustration of the synthesis of Au@Cu_2O NPs.

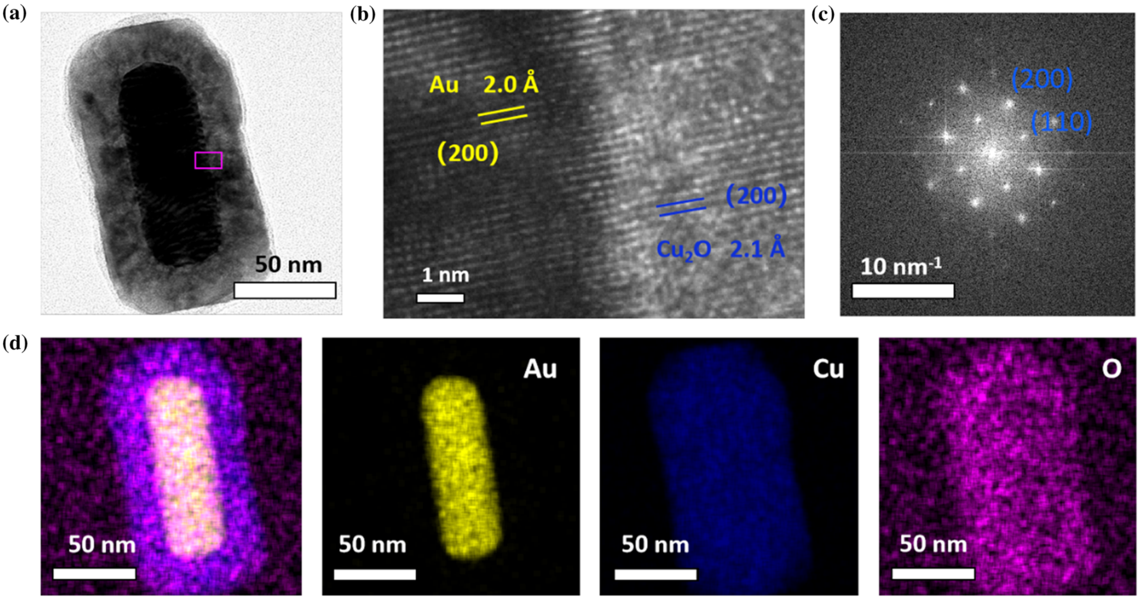

Figure 1 Characterization of the Au@Cu_2O NPs. **a** HRTEM images of a single AC-65 particle (the Au@Cu_2O with Cu_2O shell of 21 nm). **b** Interfacial HRTEM images of AC-65 sides of the red rectangular region in **a**, the (200) planes of Cu_2O were found to grow epitaxially on the (200) planes of the AuNR. **c** The corresponding FFT in marked region of Cu_2O shell shown in panel **a**. **d** EDS elemental mapping images: spatial distribution of Au, Cu and O, respectively.

energy-dispersive spectroscopy (EDS) mapping in Fig. 1d was taken to further confirm the core–shell Au@Cu_2O nanostructure.

The method that $NH_2OH{\cdot}HCl$ as a mild reducing agent reduces Cu^{2+} with binary surfactant mixtures at lower temperatures can easily grow dense and uniform Cu_2O shells over the surface of AuNRs with good coverage. Therefore, we can control the shell thickness of Cu_2O by changing the volume of Cu^{2+} added at a fixed concentration and the volume of AuNRs. A series of 0.05 M Cu^{2+} were added, namely, 35 μL, 65 μL, 100 μL, and the obtained Au@Cu_2O NPs were termed as AC-35, AC-65, and AC-100, which had increased shell thicknesses. The morphological detail of the single particle was illustrated in TEM images shown in the upper-right inset of Figs. 2a–c. Their thicknesses of Cu_2O are about 15 nm, 21 nm, and 30 nm, respectively. As shown in TEM images with a number of sample particles, each nanoparticle contained only one Au nanorod inside, and every nanostructure had very uniform shell, verifying the approach has a high productivity of monodispersed Au@Cu_2O NPs.

The relation between the optical properties of Au@Cu_2O NRs and the shell thickness was further explored by taking the UV–vis absorption spectra of AuNRs and Au@Cu_2O NRs with different shell thicknesses. The extinction spectra of AuNRs, AC-35, AC-65, and AC-100 were shown in Fig. 3a, which were measured at the same concentration. Compared with the bare AuNRs, the extinction spectra of Au@Cu_2O NRs are abundant but intensity has an apparent decrease, which means covering the Cu_2O shell over the AuNRs surface weakened surface plasmon resonance, especially the longitudinal plasmonic peak. With the increase of the Cu_2O shell thickness, this longitudinal peak is more and more apparent and has a slight red-shift, owing to a large permittivity of Cu_2O ($\varepsilon \sim 7$) [36]. Au@Cu_2O crystals have a characteristic absorption peak at ~ 500 nm arising from the scattering of the Cu_2O shell [37]. It's worth noting that two transverse plasmonic peaks, signed as peak1 and peak2 in Fig. 3a, were observed, which originated from an octupole plasmon resonance mode and the transverse dipole plasmon mode, respectively [37]. Two transverse plasmon peaks produces maybe due to the component, the AR, or existing gap and so on [38]. In this structure, we infer that the Cu_2O shell with different thicknesses is the major factor. The intensity and wavelength of two peaks were extracted and drawn as a function of Cu^{2+} amount in a line chart of Figs. 3b and c. The red-shift trend of peak1 and peak2 is same as the longitudinal plasmon peak. It is interesting that

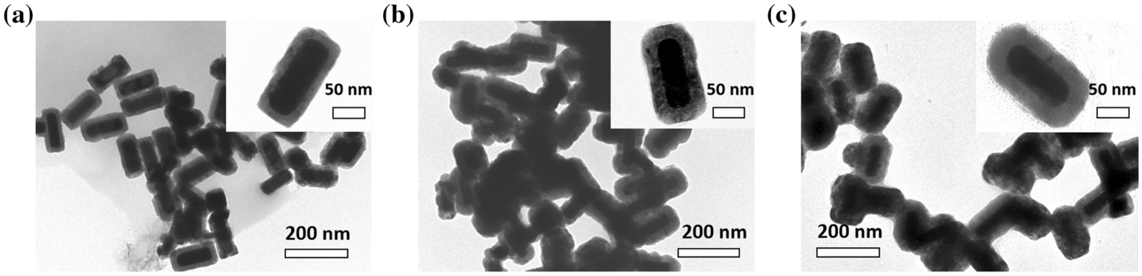

Figure 2 Au@Cu_2O nanocomposite samples with varying Cu_2O shell thicknesses. TEM images of **a** AC-35; **b** AC-65; **c** AC-100, which were produced by changing the volume of $CuCl_2{\cdot}2H_2O$ (0.05 M) from 35 μL to 65 μL, and 100 μL, respectively. Insets: enlarged pictures of the single Au@Cu_2O particle. The average lengths/widths of AC-35, AC-65, AC-100 were 143 ± 10 nm/67 ± 6 nm, 153 ± 13 nm/81 ± 11 nm, 175 ± 12 nm/98 ± 8 nm.

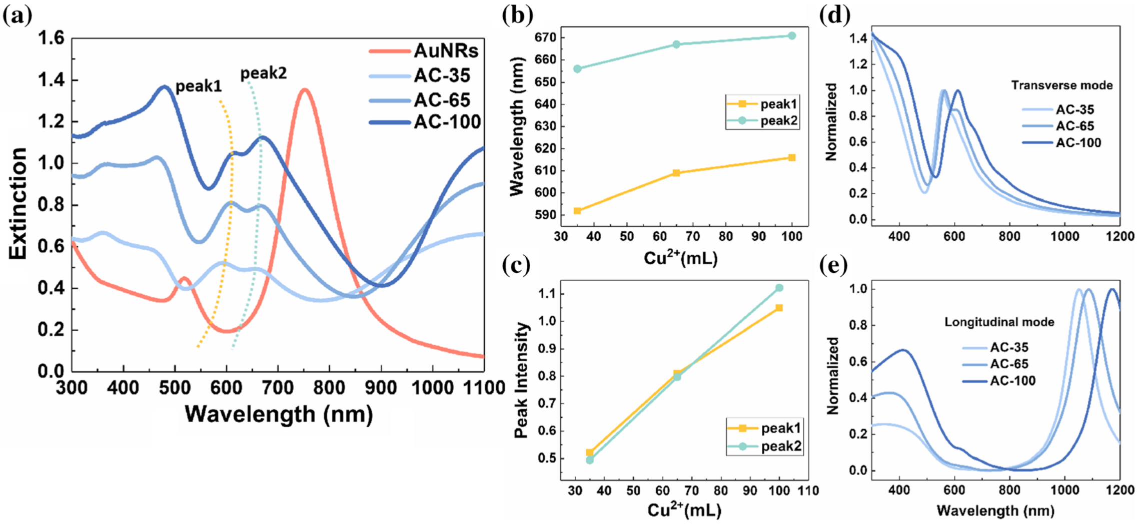

Figure 3 Extinction spectra of Au@Cu_2O NPs obtained in experiment and simulation. **a** UV–vis extinction spectra of the AuNRs and Au@Cu_2O NPs synthesized with different amounts of 0.05 M Cu^{2+} (35 μL, 65 μL, 100 μL, respectively). **b** Plots of the peak wavelength with Cu^{2+} concentration. **c** Plots of the peak intensity with Cu^{2+} concentration. **d** FDTD simulated extinction spectra of Au@Cu_2O NPs with different shell thicknesses in transverse modes. **e** FDTD simulated extinction spectra of Au@Cu_2O NPs with different shell thicknesses in longitudinal modes.

the intensity of peak1 weakened and the intensity of peak2 strengthened as the volume of Cu^{2+} increases, and the intensity of both two peaks were similar when Cu^{2+} added is 65 μL.

To verify the plasmonic properties of the Au@Cu_2O nanostructures, we simulated the absorption spectra of single nanoparticle with different Cu_2O shell thicknesses in transverse and longitudinal LSPR modes. In Fig. 3d, transverse mode of single Au@Cu_2O with different Cu_2O shell thicknesses was normalized by the peak1. We found the tendency of the two transverse peaks gradually appeared and then it became weaker with the increasing of Cu_2O shell thickness. The extinction spectra in Fig. 3e, normalized by the longitudinal peak, shows the longitudinal peak of Au@Cu_2O with increasing Cu_2O shell has a slight red-shift. Perfect narrow spectra were obtained in FDTD simulations, while the broadening and dampening of experimental LSPRs were observed. This is owing to the polydispersity of nanoparticles in water solution, but the simulation used the model of single particle. Although so, the change tends of plasmonic peaks calculated are in good agreement with the experimental data.

To further investigate the anisotropic effect on the extinction spectra, we have performed FDTD simulations of Au@Cu_2O with aspect ratio (AR) of 1, 2, 3, and 4, respectively. Figure S4 show the spectra of transverse (Figure S4a) and longitudinal (Figure S4b) LSPR mode of Au@Cu_2O with different AR of

AuNRs. The shell thickness of Cu_2O was set to be 20 nm in all simulations. For the case of AR = 1 (spheres), only one transverse peak appeared. With the increase of AR, the transverse mode became broaden and two obvious peaks appeared. For the longitudinal mode of AR = 1 (spheres), limited red-shift was observed. With the increase of AR (more anisotropic), the peak quickly red-shifted to near-infrared region (AR = 4, ~ 1300 nm). The simulated extinction spectra of Au@Cu_2O nanosphere (AR = 1) and Au@Cu_2O nanoparticles with AR of 2, 3, 4 reflected that anisotropic shape influence both the transverse and longitudinal LSPR modes.

MO as an azoic dye used on industrial scale has one or more azo bonds and aromatic rings, which is extremely stable under illumination or washing. It is helpful for textile or dye industries whereas its wastewater is harmful to biological ecosystems, such as carcinogenic and mutagenic. The azo dyes aqueous solution is highly colored even though at a low concentration [39]. Therefore, it is necessary to focus and try to solve this problem.

The catalytic activity of Au@Cu_2O NPs was investigated by catalytic reduction of MO in the present of $NaBH_4$. MO is orange and its characteristic peak is at 464 nm in water. As MO is gradually reduced, the solution will be faded to colorless and the intensity of the characteristic peak will descend, which can be monitored by the UV–vis absorption spectra. MO can be reduced by $NaBH_4$, but this process is extremely slow. The time-dependent UV–vis absorption spectra were displayed in Figure S5a, in which the intensity of the characteristic peak dropped slowly and it is difficult to react completely. Then, nanoparticles, including AuNRs, AC-35, AC-65, and AC-100 were used as catalysts to reduce MO. Figure S5b and Figs. 4a-c recorded the temporal evolution of MO adsorption spectra using these particles as catalysts, and the total time of the reduction reaction respectively were 24 min, 13 min, 9 min, and 10 min. The rate of reaction using AuNRs was still low, while the rate using Au@Cu_2O NPs had a significant improvement. Usually, we predict the reaction time shortens as the shell thickness increases. More added Cu^{2+} means a larger contact area, because we synthesized Au@Cu_2O NPs using an equal number of Au as core. However, AC-65 reduced MO in the shortest time, which doesn't own the thickest shell. Hence, we infer a too thick shell is a disadvantage to catalyzing.

Therefore, we further tested the reaction time using pure Cu_2O NPs as catalysts in comparison with Au@Cu_2O NPs, the time-dependent UV–vis adsorption spectra are shown in Fig. 4d. The TEM image and extinction spectra of Cu_2O NPs are displayed in Figure S6. The pseudo-first-order kinetics equation was applied to compare the rate of reaction. In Fig. 4e, the equation $-\ln(C/C_0) = kt$, was used to calculate and plot the rate constant according to Fig. 4 and Figure S5, where C is the MO concentration at reaction time t, C_0 is the initial MO concentration and k is the rate constant. Apparently, the most active catalyst is AC-65, and then is AC-100, AC-35. Pure Cu_2O particles have a better catalytic property than pure Au one, which means Cu_2O plays a more crucial role in this hybrid nanostructure to catalyze MO reduction reaction. To avoid the effect of $NaBH_4$ and make the rules universal, we repeated these experiments more than 3 times, and the catalytic rate and conversion with or without catalysts were exhibited in Figure S7 and Fig. 4f. Specifically, the rate of AC-65 is ~ 22 times than that of the AuNRs and ~ 4 times that of the Cu_2O NPs. The catalytic efficiency is 124% or 32% higher than the AC-35 or AC-100. The MO was completely converted using three kinds of Au@Cu_2O NPs. The conversion of Cu_2O was approaching 90%, while the conversion without catalyst and with AuNRs only was 39% and 51%, respectively. We found that single-component nanostructures of AuNRs and Cu_2O do not perform good catalytic activities. Hence, it is speculated that the perfect catalytic activity of Au@Cu_2O NPs is attributed to the synergistic effect of Au and Cu_2O. Within a certain thickness, the thicker shell has the better catalytic property. Once out of the range, the performance of Au@Cu_2O nanoparticles is similar to the pure Cu_2O particles, making the catalytic properties weak. It is noteworthy that metal–semiconductor nanostructure is a series of excellent catalysts for dye degradation, and our Au@Cu_2O nanostructures show excellent catalytic performances. Zhou's group [12] have synthesized AuNRs coating with the mesoporous SnO_2 shell to catalytic reduce 4-nitrophenol, and their catalytic activity are 3–5 times faster than that of the pure AuNRs. Gao et al. [40] have used Fe_3O_4/Au NPs to degrade MO assisted by H_2O_2 as oxidant. The rate of reduction reaction enhanced 7 times compared to the Fe_3O_4 + Au NPs mixture as catalysts.

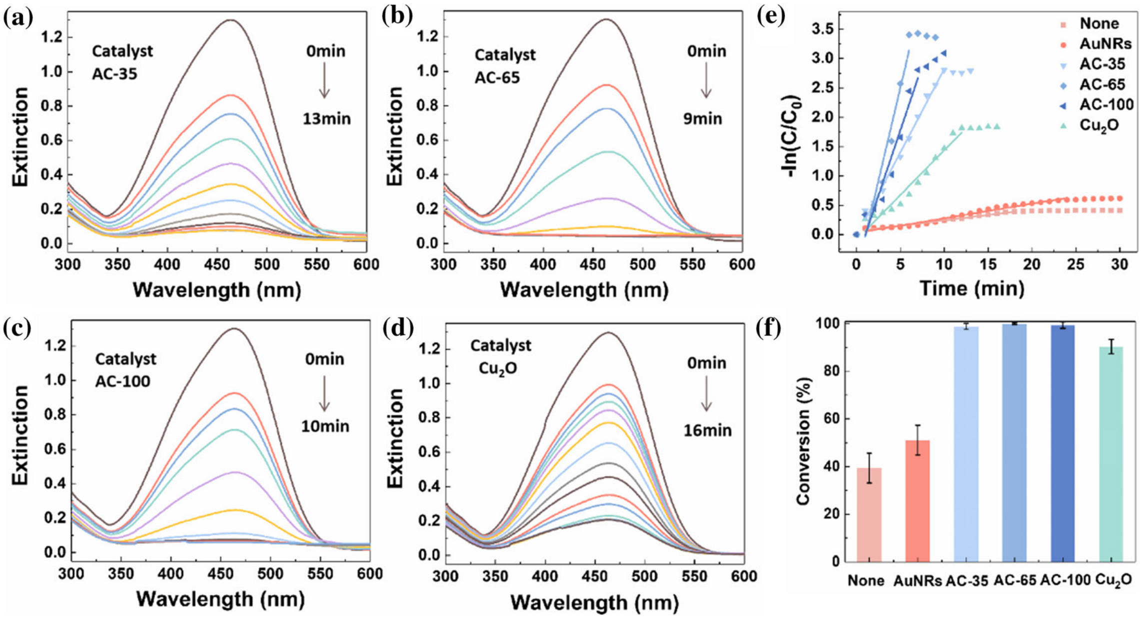

Figure 4 Time-dependent UV–vis absorption spectra of the reduction of MO by $NaBH_4$ using different nanoparticles as catalysts: **a** AC-35: Au@Cu_2O NPs with 15 nm Cu_2O shell; **b** AC-65: Au@Cu_2O NPs with 21 nm Cu_2O shell; **c** AC-100: Au@Cu_2O NPs with 30 nm Cu_2O shell; **d** Cu_2O NPs. **e** Kinetic linear fitting curves for the reduction of MO of different catalysts (no catalyst; AuNRs; Au@Cu_2O NPs with three different sizes; Cu_2O). **f** Conversion for the reduction of MO of different catalysts.

A mechanism of catalytic activity on Au@Cu_2O NPs was proposed, the energy band diagram, and catalytic reduction process were illustrated in Fig. 5. It is the Schottky barrier that is helpful for electron–hole separation to render Au@Cu_2O NPs having the outstanding catalytic effects. When metal and semiconductor are in contact, the Schottky barrier may be constructed, depending on the work function of the metal and semiconductor. The Schottky barrier can be formed only satisfying a prerequisite that: the work function of the semiconductor is significantly larger than the work function of metal, which allows for the electron to spill out from metal to semiconductor. The work function of Au is 5.1 eV. Owing to the *p*-type Cu_2O, the work function of Cu_2O depends on its crystal facets [41]. The Fermi level of Cu_2O (110) almost has no difference with Au. Therefore, a low or no Schottky barrier for holes forms between

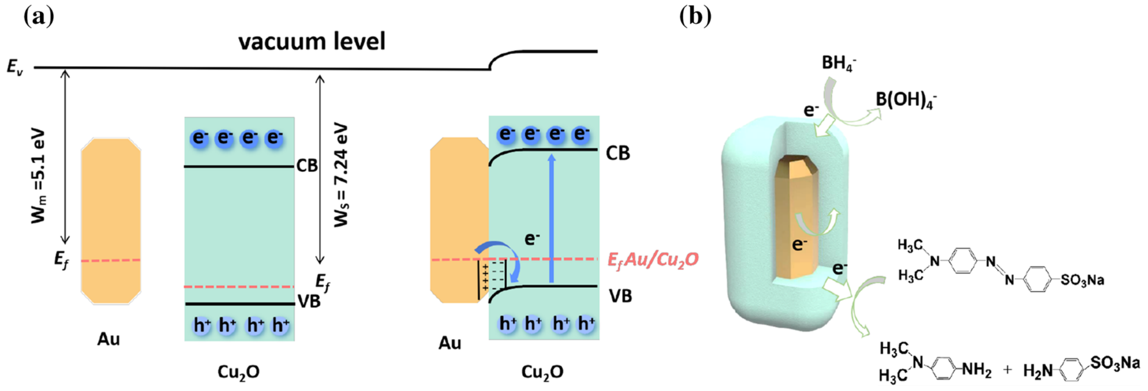

Figure 5 Schematics for mechanisms of Au@Cu_2O catalysis. **a** Energy band diagram between Au and Cu_2O of Au@Cu_2O. (Wm, Ws respectively represents the work function of Au and Cu_2O, *Ev* is zero potential energy in vacuum, E_f is Fermi energy level, CB is the conduction band, and VB is the valence band.) **b** The catalytic reduction theory for MO over the Au@Cu_2O particle.

Cu_2O (110) and Au [42]. But the work function of Cu_2O (200) is 7.2 eV, suggesting that electrons prefer to transfer from Au to Cu_2O {200} facets, which mainly improves the catalytic activities of Au@Cu_2O NPs [41]. When a Schottky junction is formed, it expedites the migration of electrons. The energy band of Au and Cu_2O is curved. The Fermi level of Au goes down, and the Fermi level of Cu_2O raises up, until they are equal and an inner electric field between Au and Cu_2O is established. The Schottky junction construction at the interface can prevent the electrons from transferring back to Au, which is beneficial to restrain the recombination of $e^- - h^+$ pairs and further boost the catalytic ability. $NaBH_4$ is attached to the valence band of Cu_2O and supplies electrons to drive the catalytic reaction. At the same time, electrons in Cu_2O transfer from the valence band to the conduction band, and the electrons gathered at the CB of Cu_2O can capture and reduce MO, as illustrated in Fig. 5b. It is Au@Cu_2O particles that offer a platform to attach BH_4^- ions and MO molecules and synergistically accelerate the charge migration from Au to Cu_2O for finally transferring from $NaBH_4$ to MO.

Summary and conclusion

In summary, we have synthesized Au@Cu_2O NPs by a simple method with binary surfactant mixtures at lower temperatures, leading to good coverage and crystalline of Cu_2O on AuNR. The synthesized Au@Cu_2O NPs are core–shell structures and the interface between the Au core and Cu_2O shell was found to be epitaxial. The size control of Au@Cu_2O was achieved by changing the volume of $CuCl_2 \cdot 2H_2O$ precursor. The prepared Au@Cu_2O NPs exhibited two transverse LSPR modes, and their intensity are related to the thickness of Cu_2O shells. In addition, the catalytic performance of all the obtained Au@Cu_2O NPs was explored by reducing MO with the aid of $NaBH_4$. AC-65 shows better catalytic efficiency than AC-35 and AC-100, which means the synergistic effect improves the properties of catalysts but too thick Cu_2O shells weaken the catalytic properties of Au@Cu_2O composites. Compared with AuNRs and Cu_2O NPs, Au@Cu_2O composites significantly promoted the reaction rate due to the Schottky barrier formed at the interface of Au and Cu_2O can effectively prevent the reconstruction of electron–hole pairs. Therefore, the Au@Cu_2O nanostructures we produced which Cu_2O shells could be controlled have great potential for future catalytic fields.

Supplementary information

See the supplementary material for TEM images and extinction spectra of AuNRs and Cu_2O nanoparticles, Additional TEM, HRTEM and HAADF-STEM images of Au@Cu_2O, FDTD simulation of Au@Cu_2O NPs with different AR of AuNRs, the catalytic process of MO by $NaBH_4$ and AuNRs, the reaction rate of different catalysts.

Acknowledgements

The authors thank Sudan Shen for her assistance in TEM at State Key Laboratory of Chemical Engineering (Zhejiang University). The authors also acknowledge financial support from National Natural Science Foundation of China (NSFC, Grant No. 61905056). This work was also supported by National Key R&D Program of China (Grant:2018YFE0207500), the National Natural Science Foundation (Grant 91938201 and 61871169), Zhejiang Provincial Natural Science Foundation (Grant LZ20F010004) and Project of Ministry of Science and Technology (Grant D20011).

Author contributions

Y-QD: Investigation; Writing – original draft; Visualization. T-SD: Writing – review & editing; Funding acquisition; Supervision. QZ: Investigation. X-YZ: Resources. JL: Writing – review & editing; Resources. Z-QC: Funding acquisition.

Declarations

Conflict of interest The authors declares that they have no conflict to interest.

Supplementary Information: The online version contains supplementary material available at https://doi.org/10.1007/s10853-023-08524-1.

References

[1] Ha M, Kim J-H, You M et al (2019) Multicomponent plasmonic nanoparticles: from heterostructured nanoparticles to colloidal composite nanostructures. Chem Rev 119:12208–12278. https://doi.org/10.1021/acs.chemrev.9b00234

[2] Zhou M, Li C, Fang J (2021) Noble-metal based random alloy and intermetallic nanocrystals: syntheses and applications. Chem Rev 121:736–795. https://doi.org/10.1021/acs.chemrev.0c00436

[3] Xie C, Niu Z, Kim D et al (2020) Surface and interface control in nanoparticle catalysis. Chem Rev 120:1184–1249. https://doi.org/10.1021/acs.chemrev.9b00220

[4] Yoo S, Lee J, Hilal H et al (2022) Nesting of multiple polyhedral plasmonic nanoframes into a single entity. Nat Commun 13:4544. https://doi.org/10.1038/s41467-022-32261-9

[5] Zhang Q, Deng T-S, Wei M-Z et al (2021) Symmetric and asymmetric overgrowth of a Ag shell onto gold nanorods assisted by Pt pre-deposition. RSC Adv 11:34516–34524. https://doi.org/10.1039/D1RA07415F

[6] van der Hoeven JES, Jelic J, Olthof LA et al (2021) Unlocking synergy in bimetallic catalysts by core–shell design. Nat Mater 20:1216–1220. https://doi.org/10.1038/s41563-021-00996-3

[7] Zhang X, Han B, Wang Y et al (2019) Catalysis of organic pollutants abatement based on Pt-decorated Ag@Cu_2O heterostructures. Molecules 24:2721. https://doi.org/10.3390/molecules24152721

[8] Yong Z, Shi Q, Fu R, Cheng W (2021) Fine-tuning Au@Pd nanocrystals for maximum plasmon-enhanced catalysis. Adv Mater Interfaces 8:2001686. https://doi.org/10.1002/admi.202001686

[9] Huang J, Zhou T, Zheng H et al (2022) Construction of ternary multifunctional Fe_3O_4/Cu_2O/Au nanocomposites: SERS detection and visible light driven photocatalysis for organic dyes. Ceram Int 48:25413–25423. https://doi.org/10.1016/j.ceramint.2022.05.216

[10] Wang B, Li R, Zhang Z et al (2017) Novel Au/Cu2O multi-shelled porous heterostructures for enhanced efficiency photoelectrochemical water splitting. J Mater Chem A 5:14415–14421. https://doi.org/10.1039/C5TA06869J

[11] Sayed M, Yu J, Liu G, Jaroniec M (2022) Non-noble plasmonic metal-based photocatalysts. Chem Rev 122:10484–10537. https://doi.org/10.1021/acs.chemrev.1c00473

[12] Zhou N, Polavarapu L, Wang Q, Xu Q-H (2015) Mesoporous SnO_2 -coated metal nanoparticles with enhanced catalytic efficiency. ACS Appl Mater Interfaces 7:4844–4850. https://doi.org/10.1021/am508803c

[13] de Ruíz-Baltazar ÁJ (2021) Sonochemical activation-assisted biosynthesis of Au/Fe_3O_4 nanoparticles and sonocatalytic degradation of methyl orange. Ultrason Sonochem 73:105521. https://doi.org/10.1016/j.ultsonch.2021.105521

[14] Zhao S, Riedel M, Patarroyo J et al (2022) Tailoring of the photocatalytic activity of CeO_2 nanoparticles by the presence of plasmonic Ag nanoparticles. Nanoscale 14:12048–12059. https://doi.org/10.1039/D2NR01318E

[15] Wei M-Z, Deng T-S, Zhang Q et al (2021) Seed-mediated synthesis of gold nanorods at low concentrations of CTAB. ACS Omega 6:9188–9195. https://doi.org/10.1021/acsomega.1c00510

[16] González-Rubio G, Díaz-Núñez P, Rivera A et al (2017) Femtosecond laser reshaping yields gold nanorods with ultranarrow surface plasmon resonances. Science 358:640–644. https://doi.org/10.1126/science.aan8478

[17] Fedorczyk A, Ratajczak J, Kuzmych O, Skompska M (2015) Kinetic studies of catalytic reduction of 4-nitrophenol with NaBH4 by means of Au nanoparticles dispersed in a conducting polymer matrix. J Solid State Electrochem 19:2849–2858. https://doi.org/10.1007/s10008-015-2933-5

[18] Zhao P, Feng X, Huang D et al (2015) Basic concepts and recent advances in nitrophenol reduction by gold- and other transition metal nanoparticles. Coord Chem Rev 287:114–136. https://doi.org/10.1016/j.ccr.2015.01.002

[19] Liu J, You F, He B et al (2022) Directing the architecture of surface-clean Cu_2O for CO electroreduction. J Am Chem Soc 144:12410–12420. https://doi.org/10.1021/jacs.2c04260

[20] Chen X, Cui K, Hai Z et al (2021) Hydrothermal synthesis of Cu_2O with morphology evolution and its effect on visible-light photocatalysis. Mater Lett 297:129921. https://doi.org/10.1016/j.matlet.2021.129921

[21] Kumar A, Singh H, Sahay S, Balasubramanian KB (2022) Charge injection Into electrodeposited Cu_2O from metallic stacks and graphene. IEEE Trans Electron Devices 69:5755–5759. https://doi.org/10.1109/TED.2022.3197380

[22] Guo L, Mao Z, Jin S et al (2021) A SERS study of charge transfer process in Au nanorod-MBA@Cu_2O assemblies: effect of length to diameter ratio of Au nanorods. Nanomaterials 11:867. https://doi.org/10.3390/nano11040867

[23] Zhang S, Yi W, Guo Y et al (2021) Driving click reactions with plasmonic hot holes on (Au Core)@(Cu_2O Shell) nanostructures for regioselective production of 1,2,3-Triazoles. ACS Appl Nano Mater 4:4623–4631. https://doi.org/10.1021/acsanm.1c00220

[24] Zhang G, Ma Y, Liu F et al (2021) Seeded growth of Au@Cu_xO core-shell mesoporous nanospheres and their

photocatalytic properties. Front Chem 9:671220. https://doi.org/10.3389/fchem.2021.671220

[25] Wu T, Zheng H, Kou Y et al (2021) Self-sustainable and recyclable ternary Au@Cu2O–Ag nanocomposites: application in ultrasensitive SERS detection and highly efficient photocatalysis of organic dyes under visible light. Microsyst Nanoeng 7:23. https://doi.org/10.1038/s41378-021-00250-5

[26] Zhu Y, Hong W, Liu X et al (2021) Rapid bacterial elimination achieved by sonodynamic Au@Cu_2O hybrid nanocubes. Nanoscale 13:15699–15710. https://doi.org/10.1039/D1NR04512A

[27] Zhang A, Liu Y, Wu J et al (2022) Weakening OO binding on Au-Cu_2O/carbon nanotube catalysts with local misfit dislocation by interfacial coupling interaction for oxygen reduction reaction. Chem Eng Sci 252:117513. https://doi.org/10.1016/j.ces.2022.117513

[28] Huang Y, Han Y, Sun J et al (2022) Dual nanocatalysts co-decorated three-dimensional, laser-induced graphene hybrid nanomaterials integrated with a smartphone portable electrochemical system for point-of-care non-enzymatic glucose diagnosis. Mater Today Chem 24:100895. https://doi.org/10.1016/j.mtchem.2022.100895

[29] Chen Y, Lin P, Zou X et al (2022) Machine-learning-aided identification of steroid hormones based on the anisotropic galvanic replacement generated sensor array. Sens Actuators B Chem 370:132470. https://doi.org/10.1016/j.snb.2022.132470

[30] Lu B, Liu A, Wu H et al (2016) Hollow Au–Cu_2O core-shell nanoparticles with geometry-dependent optical properties as efficient plasmonic photocatalysts under visible light. Langmuir 32:3085–3094. https://doi.org/10.1021/acs.langmuir.6b00331

[31] Kong L, Chen W, Ma D et al (2012) Size control of Au@Cu_2O octahedra for excellent photocatalytic performance. J Mater Chem 22:719–724. https://doi.org/10.1039/C1JM13672K

[32] Xu W, Jia J, Wang T et al (2020) Continuous tuning of Au–Cu_2O janus nanostructures for efficient charge separation. Angew Chem Int Ed 59:22246–22251. https://doi.org/10.1002/anie.202010613

[33] Ye X, Zheng C, Chen J et al (2013) Using binary surfactant mixtures to simultaneously improve the dimensional tunability and monodispersity in the seeded growth of gold nanorods. Nano Lett 13:765–771. https://doi.org/10.1021/nl304478h

[34] Palik ED, Ghosh G (1998) Handbook of optical constants of solids. Academic Press, San Diego

[35] Kuo C-H, Huang MH (2008) Facile synthesis of Cu_2O nanocrystals with systematic shape evolution from cubic to octahedral structures. J Phys Chem C 112:18355–18360. https://doi.org/10.1021/jp8060027

[36] Zhang L, Jing H, Boisvert G et al (2012) Geometry control and optical tunability of metal-cuprous oxide core-shell nanoparticles. ACS Nano 6:3514–3527. https://doi.org/10.1021/nn300546w

[37] Zhang S, Jiang R, Guo Y et al (2016) Plasmon modes induced by anisotropic gap opening in Au@Cu2O nanorods. Small 23:4264–4276. https://doi.org/10.1002/smll.201600065

[38] Hu Z, Mi Y, Ji Y et al (2019) Multiplasmon modes for enhancing photocatalytic activity of Au/Ag/Cu_2O core-shell nanorods. Nanoscale 11:16445–16454. https://doi.org/10.1039/c9nr03943k

[39] Muhd Julkapli N, Bagheri S, Bee Abd Hamid S (2014) Recent advances in heterogeneous photocatalytic decolorization of synthetic dyes. Sci World J 2014:1–25. https://doi.org/10.1155/2014/692307

[40] Gao Q, Xing Y, Peng M et al (2017) Enhancement of Fe_3O_4/Au composite nanoparticles catalyst in oxidative degradation of methyl orange based on synergistic effect. Chin J Chem 35:1431–1436. https://doi.org/10.1002/cjoc.201700032

[41] Wang L, Ge J, Wang A et al (2014) Designing p-type semiconductor-metal hybrid structures for improved photocatalysis. Angew Chem Int Ed 53:5107–5111. https://doi.org/10.1002/anie.201310635

[42] Yanagida S, Yajima T, Takei T, Kumada N (2022) Removal of hexavalent chromium from water by Z-scheme photocatalysis using TiO_2 (rutile) nanorods loaded with Au core–Cu_2O shell particles. J Environ Sci 115:173–189. https://doi.org/10.1016/j.jes.2021.05.025

Supporting Information

A study of size-controlled Au@Cu_2O nanocomposite for highly improved methyl orange catalytic performances

Yun-Qi Dou[†], *Tian-Song Deng*[†, *], *Qi Zhang*[†], *Xiaoyu Zhao*[‡], *Jia Liu*[‡], *Zhiqun Cheng*[†]

[*] *Corresponding author. E-mail: dengts@pku.edu.cn*

[†] School of Electronics and Information Engineering, Hangzhou Dianzi University, Hangzhou 310018, P. R. China.

[‡] College of Materials and Environmental Engineering, Hangzhou Dianzi University, Hangzhou 310018, P. R. China.

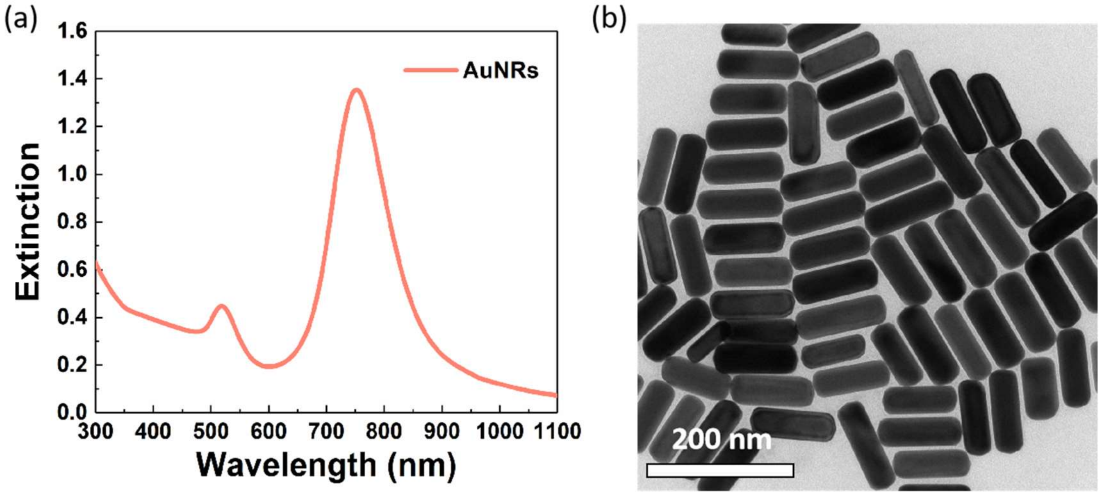

Figure S1. Extinction spectra (a) and TEM image (b) of AuNRs, having the longitudinal LSPR peaks at 752 nm. Their average lengths of AuNRs are 112 ± 9 nm, and widths are 38 ± 2 nm.

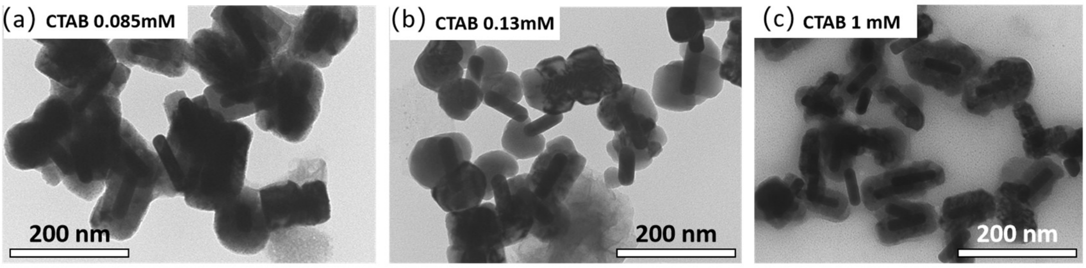

Figure S2. TEM images of Au@Cu_2O NPs, synthesized with different concentrations of CTAB.

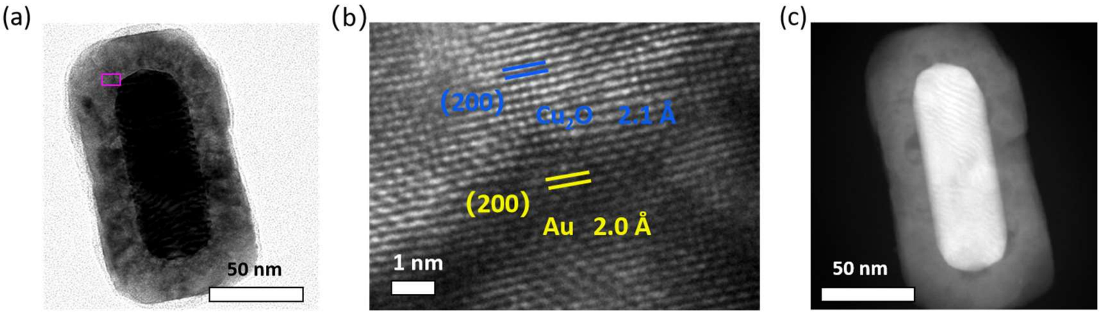

Figure S3. (a) HRTEM images of single AC-65 particle (the Au@Cu_2O with Cu_2O shell of 21 nm). (b) Interfacial HRTEM images (red square regions) on sides of AC-65 in (a). (c) The HAADF-STEM image of a single AC-65 particle.

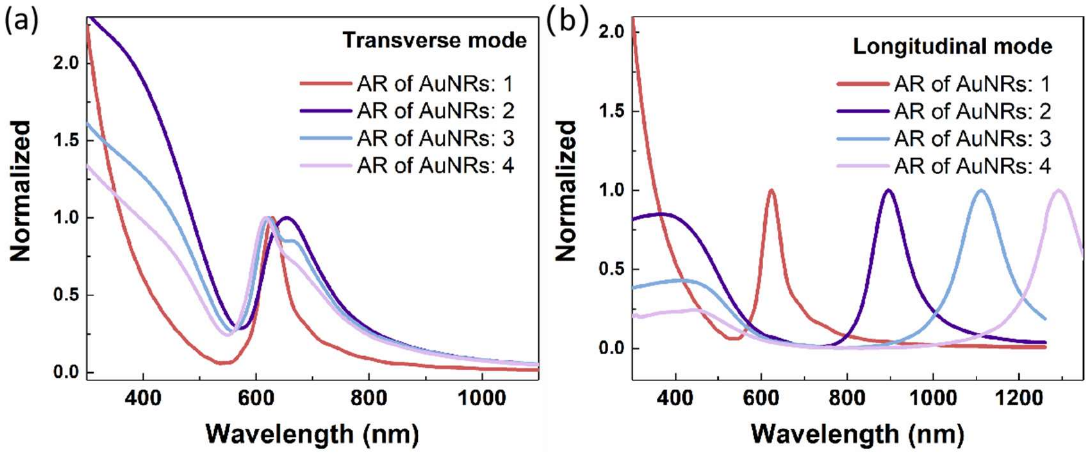

Figure S4. (a) FDTD simulated extinction spectra of Au@Cu_2O NPs with different AR of AuNRs in transverse mode. The spectra were normalized by the peak1. (b) FDTD simulated extinction spectra of Au@Cu_2O NPs with different AR in longitudinal mode. The spectra were normalized by the longitude peak. The length of AuNRs is changed at a fixed width of AuNRs, so that the AR of AuNRs in simulations are 1, 2, 3, 4. And the thickness of Cu_2O shell is set as 20 nm, as same as the Au@Cu_2O-65. The morphology of nanostructure that the AR=1 of AuNRs is namely Au@Cu_2O nanosphere.

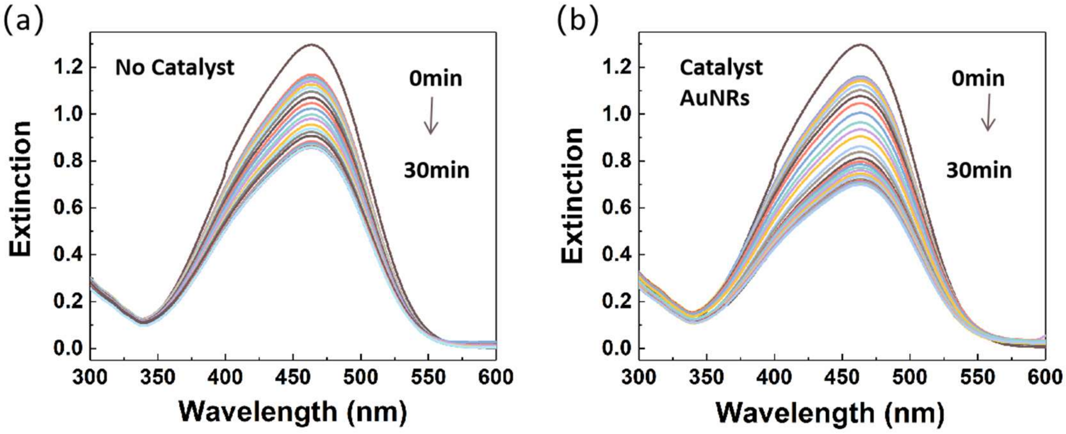

Figure S5. Time-dependent UV-vis absorption spectra of the reduction of MO by $NaBH_4$ using: (a) No catalyst; (b) AuNRs.

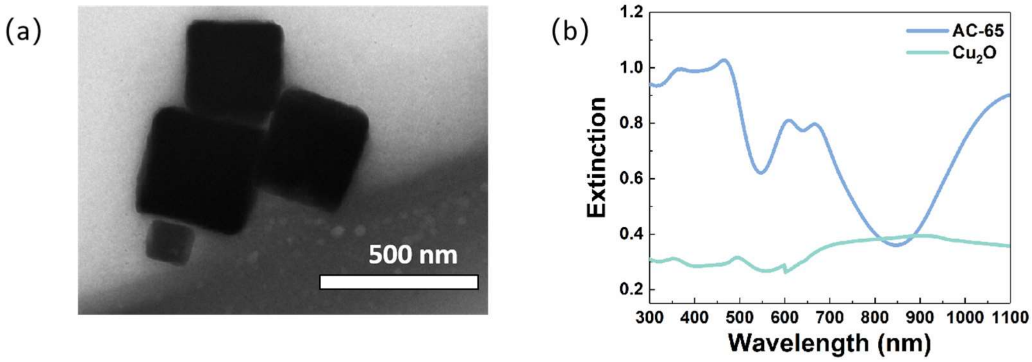

Figure S6. (a) TEM image of Cu_2O NPs; (b) UV-vis absorption spectra of Au@Cu_2O NPs and Cu_2O NPs. Two kinds of nanoparticles were synthesized by addition of 65 µL of 0.05 mM $CuCl_2 \cdot 2H_2O$

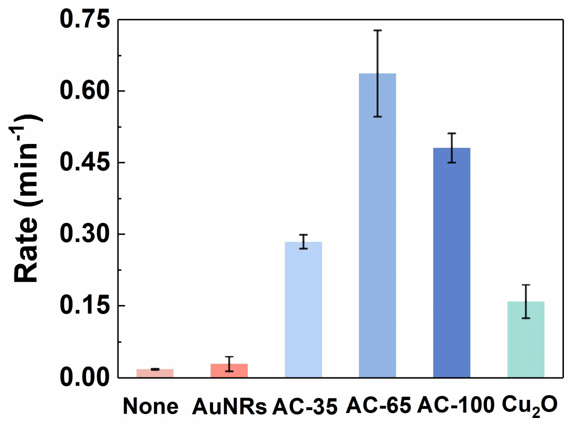

Figure S7. Comparison between the reaction rate of different catalysts: no catalyst, AuNRs, Au@Cu$_2$O NPs with three different sizes, and Cu$_2$O NPs.